





Article

Fabrication of Tungsten Oxide Nanowalls through HFCVD for Improved Electrochemical Detection of Methylamine

Mohammad Imran ^{1,2,†}, Eun-Bi Kim ^{1,†} , Tae-Geum Kim ³, Sadia Ameen ^{1,*} , Mohammad Shaheer Akhtar ^{4,5,6,*}  and Dong-Heui Kwak ^{2,*} 

¹ Advanced Materials and Devices Laboratory, Department of Bio-Convergence Science, Jeonbuk National University, Jeongeup Campus, Jeongeup 56212, Republic of Korea; mohdimran@jbnu.ac.kr (M.I.); keb821@naver.com (E.-B.K.)

² Environmental Engineering Laboratory, Department of Bioactive Material Sciences, Jeonbuk National University, Jeonju 54896, Republic of Korea

³ Department of Bio-Convergence Science, Jeonbuk National University, Jeongeup Campus, Jeongeup 56212, Republic of Korea; tgkim@jbnu.ac.kr

⁴ Graduate School of Integrated Energy-AI, Jeonbuk National University, Jeonju 54896, Republic of Korea

⁵ New & Renewable Energy Material Development Center (NewREC), Jeonbuk National University, Jeonbuk 56332, Republic of Korea

⁶ Department of JBNU-KIST Industry-Academia Convergence Research, Jeonbuk National University, Jeonju 54896, Republic of Korea

* Correspondence: sadiaameen@jbnu.ac.kr (S.A.); shaheerakhtar@jbnu.ac.kr (M.S.A.); kwak124@jbnu.ac.kr (D.-H.K.)

† These authors contributed equally to this work.

Abstract: In this study, well-defined tungsten oxide (WO₃) nanowall (NW) thin films were synthesized via a controlled hot filament chemical vapor deposition (HFCVD) technique and applied for electrochemical detection of methylamine toxic substances. Herein, for the thin-film growth by HFCVD, the temperature of tungsten (W) wire was held constant at ~1450 °C and gasification was performed by heating of W wire using varied substrate temperatures ranging from 350 °C to 450 °C. At an optimized growth temperature of 400 °C, well-defined and extremely dense WO₃ nanowall-like structures were developed on a Si substrate. Structural, crystallographic, and compositional characterizations confirmed that the deposited WO₃ thin films possessed monoclinic crystal structures of high crystal quality. For electrochemical sensing applications, WO₃ NW thin film was used as an electrode, and cyclic voltammetry (CV) and linear sweep voltammetry (LSV) were measured with a wide concentration range of 20 μM~1 mM of methylamine. The fabricated electrochemical sensor achieved a sensitivity of ~183.65 μA mM⁻¹ cm⁻², a limit of detection (LOD) of ~20 μM and a quick response time of 10 s. Thus, the fabricated electrochemical sensor exhibited promising detection of methylamine with considerable stability and reproducibility.

Keywords: WO₃; HFCVD; nanowalls; methylamine; electrochemical sensor; cyclic voltammetry; linear sweep voltammetry



Citation: Imran, M.; Kim, E.-B.; Kim, T.-G.; Ameen, S.; Akhtar, M.S.; Kwak, D.-H. Fabrication of Tungsten Oxide Nanowalls through HFCVD for Improved Electrochemical Detection of Methylamine. *Micromachines* **2024**, *15*, 441. <https://doi.org/10.3390/mi15040441>

Academic Editors: Kosuke Ino, Goreti Pereira and Giovannia A. L. Pereira

Received: 31 January 2024

Revised: 10 March 2024

Accepted: 21 March 2024

Published: 26 March 2024



Copyright: © 2024 by the authors. Licensee MDPI, Basel, Switzerland. This article is an open access article distributed under the terms and conditions of the Creative Commons Attribution (CC BY) license (<https://creativecommons.org/licenses/by/4.0/>).

1. Introduction

In today's landscape, metal oxides have emerged as valuable assets across various industries, owing to their unique chemical, physical, and electronic characteristics. Metal oxides offer versatility and find applications in a wide range of sectors, including environmental remediation [1], medical technology [2], energy solutions [3], water purification [4], and personal care product development [5]. The use of metal oxide is anticipated to grow even further, underscoring their pivotal role in advancing innovation and addressing contemporary challenges [6].

Tungsten oxide (WO₃) is a wide-band-gap metal oxide [7] which has good properties for numerous applications, e.g., information science, electronics (nano and micro), computer

science, energy (renewable and non-renewable), transportation, safety engineering, military technologies, optoelectronic [8], electrochromic devices [9] and sensing [10]. WO_3 is an n-type semiconductor which exhibits high stability, small diffusion length (150–500 nm) and good carrier mobility ($\sim 33.9 \text{ cm}^2 \text{ V}^{-1} \text{ s}^{-1}$) [11]. Tungsten oxide (WO_3) has become increasingly popular due to its superior sensitivity, heightened responsiveness to sensitization, excellent stability, and suitability for lower-temperature operations [12]. In thin-film configuration, WO_3 offers optimal electrical resistivity, selectivity, and repeatability, making it a promising candidate in sensor technology. Furthermore, it exhibits the ability to undergo changes in characteristics such as stoichiometry, composition, structure, thickness, and morphology, depending on the synthesis techniques and conditions employed [13]. WO_3 predominantly in thin films shows commendable performances due to its cost-effective properties, simple fabrication, and easy deposition process.

Various deposition techniques (vacuum and non-vacuum techniques) have been used to deposit nanostructured WO_3 thin films on substrate surfaces, including pulsed laser deposition (PLD) [14]; the electrophoresis deposition process (EDP) [15]; sputtering [16]; chemical spray pyrolysis [17]; solvothermal [18], hydrothermal [19,20], and sol-gel methods [21]; the chemical vapor deposition method [22]; and the physical vapor deposition method [23,24]. Hot filament chemical vapor deposition (HFCVD) is a cost-effective process compared to other deposition techniques. Its economic benefits arise from the use of a hot filament that decomposes preceding gases, which enables effective film development at lower temperatures [25]. It significantly minimizes the consumption of energy and instrument costs. For thin-film deposition, HFCVD is capable of depositing thin films with a high surface-to-volume ratio and intricate architectures. Accurate control enables the production of high-resolution patterns for device electrode fabrication [26]. HFCVD is beneficial for the fabrication of sensor electrodes because it can control the electrical resistivity, selectivity, and durability of thin films [27,28].

Methylamine is a hazardous organic chemical found in liquid and gas forms [29]. It is toxic, colorless, and flammable at room temperature with a typical pungent smell [30]. Methylamine is used as industrial raw material for the production of pesticides as an agriculture product, making rubbers for transportation industries, dyes for textile industries, and in pharmaceutical industries [31]. It is a hazardous chemical, and its accidental release or exposure can pose risks to public health and safety. Thus, it is crucial to monitor the presence of methylamine to ensure safety and prevent potential accidents or exposures [32]. In this regard, electrochemical detection methods can provide real-time detection and monitoring [33] of methylamine, allowing for prompt action to mitigate any risks. In particular, the chemical sensing methods enable the detection and quantification of methylamine in environmental samples [34], helping to identify potential pollution sources and assess the impact on the environment [35,36].

With these motivations, in this work, we have deposited WO_3 nanostructured thin film through HFCVD, using tungsten (W) filament in a constant O_2 pressure. The unique morphology displays WO_3 thin-film nanowalls (WO_3 NWs) with a grain size of 20–25 nm. To the best of our knowledge, this is the first report on single-step HFCVD-deposited WO_3 thin film with distinct morphology and has been used as an electrode material for the detection of hazardous methylamine.

2. Materials and Methods

2.1. Materials

Methylamine (CH_3NH_2 , Sigma Aldrich, $\geq 99.5\%$, St. Louis, MO, USA), silicon (Si, p-type, 10 mm \times 10 mm, Siltron Inc., Seoul, Republic of Korea), tungsten (W) wire (thickness ~ 0.5 mm, The Nilaco Corporation, Tokyo, Japan), sodium dihydrogen phosphate (NaH_2PO_4 , Sigma Aldrich, $\geq 99\%$, St. Louis, MO, USA), and disodium hydrogen phosphate (Na_2HPO_4 , Sigma Aldrich, $\geq 99\%$, St. Louis, MO, USA) were used.

2.2. Synthesis of WO₃ NW Thin Film

The WO₃ NW thin film on the Si substrate was deposited through the HFCVD technique. As shown in Figure 1, the vacuum chamber is equipped with a thermocouple for measuring and monitoring the temperature, tungsten (W) wire filament was used, gas inlet pipes connected to mass flow controllers were used to regulate the flow of the gasses, and a high-current power supply, a rotary vacuum pump, and a cooling facility were attached to the vacuum chamber. For thin-film deposition, the silicon wafers (Si-P100) were cleaned with ultrasonic vibration using deionized (DI) water and acetone. Thereafter, Si substrates were placed on the substrate tray at the distance of ~10 mm from the W wire filament, and the chamber pressure was set to a constant 0.2 Torr. Subsequently, the W filament was heated at 1400 °C and the substrate temperature was raised from 300 to 450 °C for ~30 min under the supply of oxygen at a flow rate of 10 sccm. Herein, hydrogen gas was used as a precursor gas at 5.0 sccm. Finally, the W filament was oxidized at the above temperatures, resulting in the growth of WO₃ nanostructured thin film on the Si substrate.

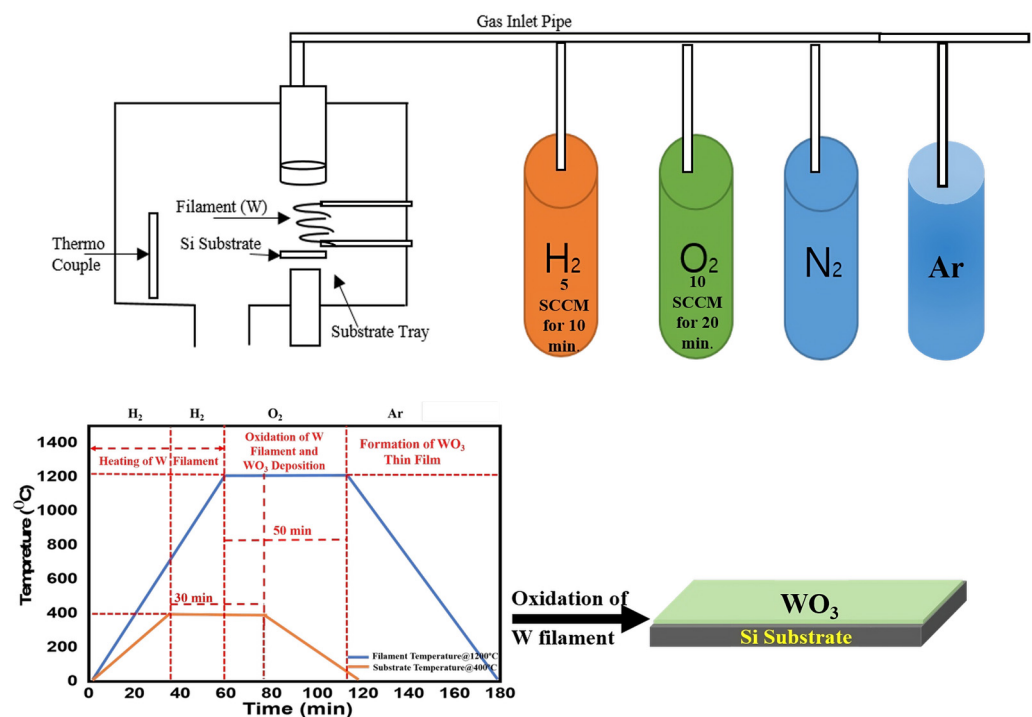


Figure 1. A schematic representation of the HFCVD process for the synthesis of WO₃ NW thin films.

2.3. Characterization Techniques

Morphological analysis was carried out by a field-emission scanning electron microscope (FESEM, Hitachi S-4700, Tokyo, Japan). The elemental composition, mapping and line scan mapping analysis were determined by the SEM-coupled energy-dispersive X-rays spectroscopy (EDS). The absorption properties were obtained through a UV–visible spectrophotometer (JASCO, V-670, Tokyo, Japan). The structural investigations of WO₃ nanostructured thin film were performed by X-ray diffraction (XRD, Rigaku, Tokyo, Japan) in the Bragg angle ranging between 20° and 60° to explain the crystal phases and lattice properties using CuK α radiation ($\lambda = 1.5406 \text{ \AA}$). Fourier-transform infrared (FTIR, Nicolet, IR300, Wisconsin, USA) was used to study bond vibrations in the range of 400–4000 cm⁻¹. X-ray photoelectron spectroscopy (XPS, KRATOS AXIS-Nova, Manchester, UK) was conducted to study the surface compositional and element states.

2.4. Sensing Performance

To detect the presence of the hazardous methylamine, a three-electrode system of 10 mL electrochemical cells was employed for the measurement of cyclic voltammetry

and linear sweep voltammetry using an electrometer (Keithley, 6517A, Aurora Rd, USA), Herein, HFCVD-grown WO₃ NW thin film served as the working electrode, AgCl/Ag was employed as a reference electrode and gold wire was utilized as the counter electrode. A targeted analyte (methylamine) was prepared at a broad concentration range of 20 μM–1 mM in a 10 mL solution of 0.1 M phosphate buffer solution (PBS) of pH 7. The use of PBS in electrochemical sensing offers advantages such as stable pH, biocompatibility, consistent ionic strength, enhanced solubility, and compatibility. Its buffering capacity and versatility make PBS a reliable choice for maintaining optimal conditions during electrochemical measurements [37]. Cyclic voltammetry was performed to study the oxidation and reduction peaks and the linear sweep voltammetry technique was used to study the current and voltage responses. The active area of the fabricated electrode was 1 cm² (WO₃ NWs) and the sensitivity was calculated by dividing the slope of the calibrated current–concentration plot by the active area of the sensor, as expressed in Equation (1):

$$\text{Sensitivity} = \frac{\text{Slope of calibrated curve}}{\text{Active area}} \quad (1)$$

Herein, CV was performed within the range of −0.8~0.8 V, with a scan rate of 50 mV/s. The current responses were analyzed within a voltage range from 0 to 2.0 V, and the response time was determined to be 10 s.

3. Results

3.1. Morphological Properties of WO₃ NW Thin Film

The morphology of HFCVD-grown WO₃ nanostructured thin films deposited on the Si substrate was investigated by FESEM and the elemental characterization was performed by energy-dispersive X-ray (EDAX). The HFCVD-grown WO₃ thin film, as shown in Figure 2a–c, depicts the formation of highly dense and uniformly distributed nanowall (NW) structures. At an optimized substrate temperature (Ts) of ~400 °C, the surface of the thin film appears notably uniform, with a grain size in the range of 20–25 nm. However, upon raising the substrate temperature, the grain size increase might be due to the increased reaction rate at the substrate surface [38]. This improved grain size might boost the overall surface area of the WO₃ thin film, indicating the availability of more active sites for chemical interactions. In the context of chemical sensing, the large surface area of the thin film brings about enhanced sensitivity, a faster response time, a low limit of detection and increases the reproducibility of the targeted electrode [39,40]. Figure 2d shows an elemental analysis of the HFCVD-grown WO₃ NW thin film, exhibiting the presence of two primary elements: W (tungsten) and O (oxygen). The EDX analysis quantifies the elemental composition, with tungsten accounting for ~24.51% and oxygen making up the remaining ~75.49%.

3.2. Optical Characterizations of WO₃ NW Thin Film

The optical properties of HFCVD-grown WO₃ NW thin film are studied by UV–vis absorption in the range of 200~800 nm. The UV–vis spectrum, as shown in Figure 3a, exhibits a sharp absorption peak at ~339 nm, which confirms the deposition of the WO₃ thin film [41,42]. The band gap value of WO₃ NW thin film is calculated by the Tauc relation:

$$\alpha = \frac{A(h\nu - E_g)^2}{h\nu} \quad (2)$$

where A, hν and E_g are a constant of proportionality, photon energy and optical bandgap energy [43], respectively. In our work, the WO₃ NW thin film has a band gap of ~3.321 eV, as shown in Figure 3b. The existence of an optical band gap energy of ~3.321 eV represents the minimum energy required to move an electron from the valence band (the highest energy band filled with electrons at absolute zero) to the conduction band (the lowest energy band with available electron states) within the thin film [44].

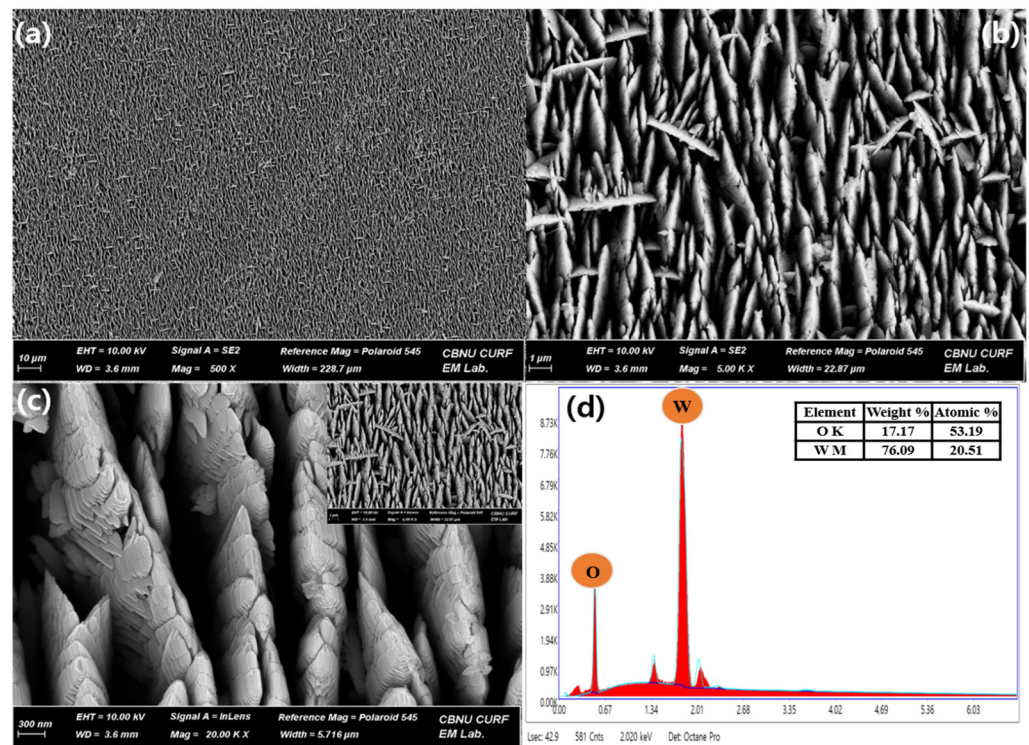


Figure 2. FESEM images (a–c) and EDX spectrum (d) of the HFCVD-grown WO₃ NW thin film.

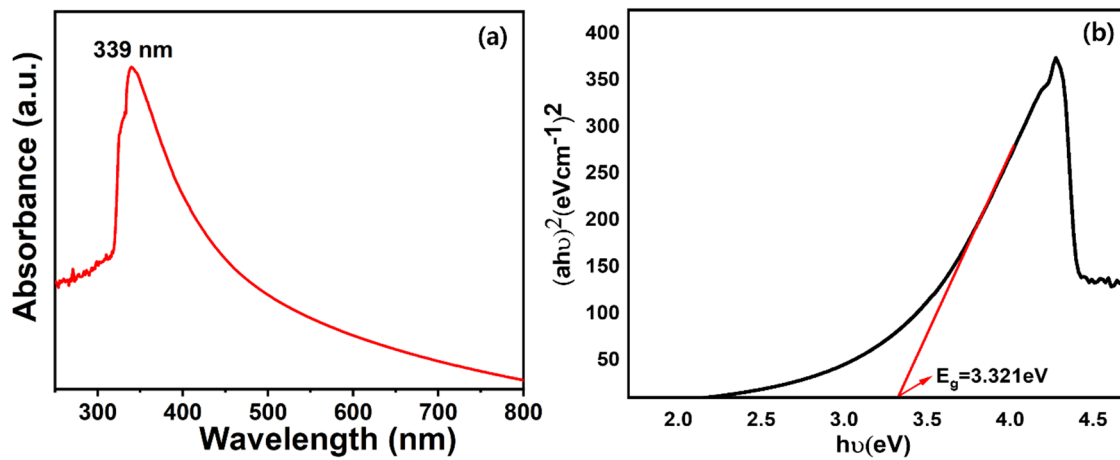


Figure 3. UV–vis spectroscopy (a) and its corresponding Tauc plot (b) of the HFCVD-grown WO₃ NW thin film.

3.3. Crystalline and Structural Studies of WO₃ NW Thin Film

XRD is performed to study the crystal structures, phases, crystallite size, and purity of the synthesized WO₃ NW thin film. Figure 4a exhibits the diffraction patterns at 23.40°, 24.54°, 26.84°, 28.91°, 33.59°, 33.89°, 34.46°, 41.78°, 45.83°, 48.61°, 50.27°, 53.78°, 54.45°, 56.09°, and 60.53° relating to miller planes (020), (200), (120), (112), (022), (202), (122), (222), (004), (020), (114), (024), (204), (142), and (320), respectively [45,46]. The obtained XRD diffraction peaks are well matched with JCPDS card no. 83-0950. The crystal size of WO₃ NW thin film is calculated as ~83.3472 nm by the Scherrer formula [47], using the most intense peak at 23.40°.

$$D = \left(\frac{k\lambda}{\beta \cos\theta} \right) \tag{3}$$

where D is the crystallite size of the particle in nm, θ is the diffraction angle, β is the full width at half maximum observed in radians (FWHM), k is the Scherrer constant ($k = 0.94$) and λ is the X-ray wavelength ($\lambda = 1.54178 \text{ \AA}$) [24,25]. Herein, the WO_3 NW thin film prepared at T_s of $\sim 400 \text{ }^\circ\text{C}$ shows phase purity at the strongest diffraction peak of 020 lattice planes, indicating the preferential growth orientation [48].

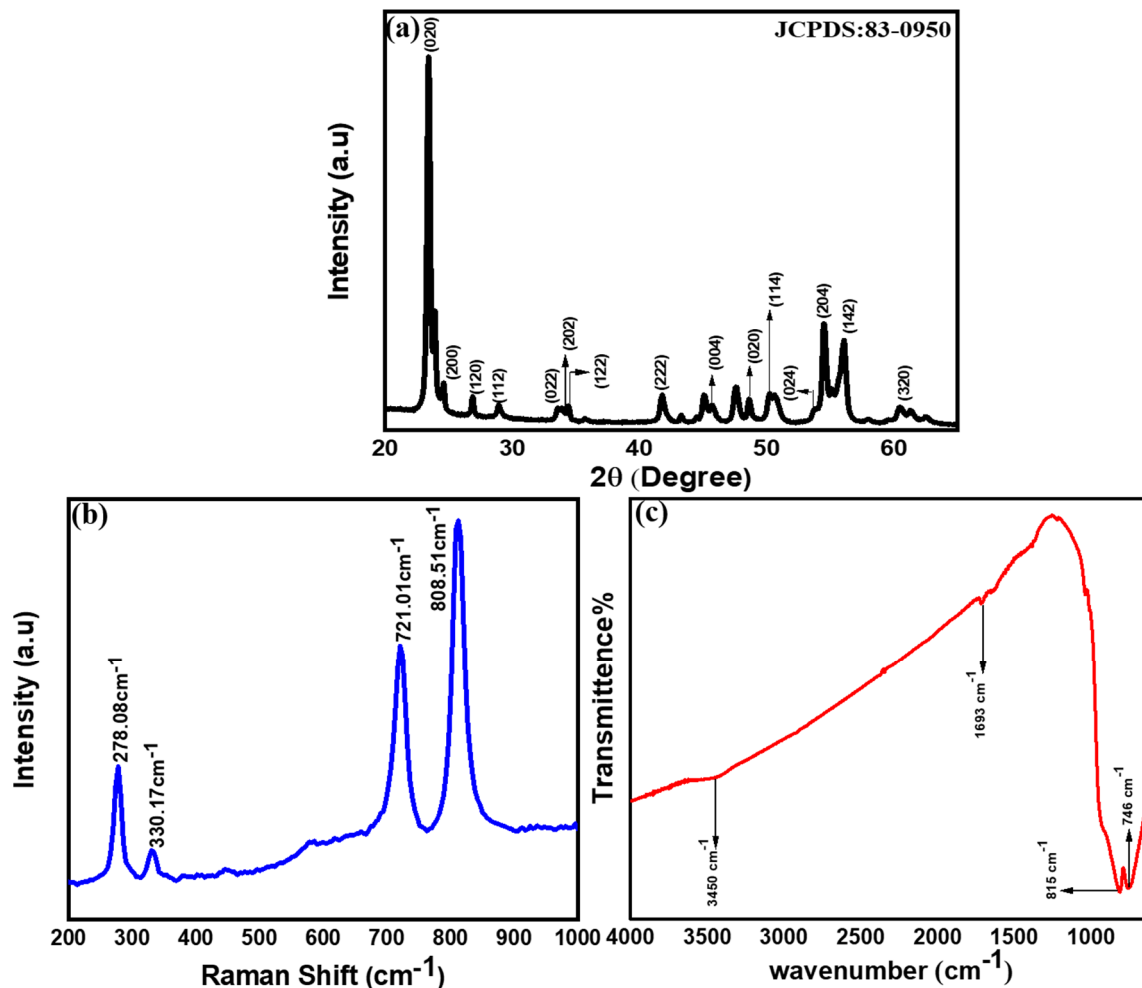


Figure 4. The XRD patterns (a), Raman spectrum (b) and FTIR spectrum (c) of HFCVD-grown WO_3 NW thin films.

Figure 4b displays the results of Raman spectroscopy, performed in the range of $200\text{--}1000 \text{ cm}^{-1}$, to measure the structural and molecular properties of the WO_3 NW thin film. Raman spectra clearly manifest the signature peaks associated with stoichiometric WO_3 with a monoclinic phase [49]. The W-O-W stretching and bending vibrations are located between 700 and 800 cm^{-1} [48] and O-W-O stretching and bending vibrations are noticed between 250 and 400 cm^{-1} [49]. The intense band at $\sim 278.08 \text{ cm}^{-1}$ and the weak band at $\sim 330.17 \text{ cm}^{-1}$ are attributed to the bending vibration of $\delta(\text{O-W-O})$ [50]. The Raman peak observed at $\sim 801 \text{ cm}^{-1}$ is the typical polycrystalline WO_3 in the monoclinic or triclinic crystalline phase [48,49].

Chemical configurations of HFCVD-grown WO_3 NW thin films at T_s of $\sim 400 \text{ }^\circ\text{C}$ is shown in Figure 4c. The spectrum exhibits transmittance in the range of $400\text{--}4000 \text{ cm}^{-1}$. The FTIR spectra exhibit a broad peak at $\sim 746 \text{ cm}^{-1}$ and 815 cm^{-1} [51], which are attributed to the stretching vibration of $\nu(\text{O-W-O})$ [51]. The $\nu(\text{O-W-O})$ stretching vibration mode is the monoclinic crystal phase, confirming that the WO_3 NW thin film is grown well on the Si substrate [52]. The transmittance peaks located at $\sim 746 \text{ cm}^{-1}$ refer to the O-W-O bending

mode of the vibration and transmittance peak located at $\sim 846\text{ cm}^{-1}$ is due to the W-O stretching mode of hexagonal WO, confirming the hexagonal structure [53].

3.4. XPS Studies of WO₃ NW Thin Films

The XPS properties provide an in-depth understanding of the oxidation states of W and O in WO₃ thin films using high-resolution spectra of W 4f and O 1s binding energies. Figure 5a showcases the fitted W4f XPS spectrum, revealing a distinct doublet pattern, with binding energies of approximately ~ 35.5 and ~ 37.7 eV [54]. These values correspond to the W 4f_{5/2} and W 4f_{7/2} electronic states, respectively. Peaks at 4f_{5/2} correspond to the binding energy of ~ 35.58 eV, aligning precisely with the characteristic energy level of the W⁶⁺ oxidation state within WO₃ thin films and indicating the predominant oxidation state of tungsten [55] in the HFCVD-grown WO₃ NW thin film. This peak serves as compelling evidence affirming that the WO₃ thin film predominantly comprise hexavalent tungsten [56]. The second distinct XPS peak emerges at approximately ~ 37.9 eV, corresponding to the 4f_{7/2} state of tungsten ions in the HFCVD-grown WO₃ NW thin film. This peak reaffirms the dominance of the W⁶⁺ oxidation state, which is crucial for understanding the electronic structure and chemical environment of the material [29,57]. Mostly, WO₃ thin films are characterized by the presence of two distinct binding energies within the range of ~ 36 – 38 eV. These binding energies are indicative of the prevalence of W⁶⁺ ions within stoichiometric WO₃ [25]. In our work, we observe a similar doublet pattern within the range of 36–38 eV, affirming the stoichiometric nature of the thin film [58,59]. The O 1s XPS plot, as depicted in Figure 5b, reveals two distinct binding energies: one with a higher intensity at ~ 530.4 eV and another with a lower intensity at ~ 531.4 and ~ 532.3 eV. Herein, the higher-intensity peak at ~ 530.2 eV typically arises from the O component of oxide, providing further evidence for the formation of W-O bonds in HFCVD-grown WO₃ NW thin films [60]. Notably, the lower-energy peaks at ~ 531.4 and ~ 532.3 eV are associated with -OH or H₂O species on the thin film's surface, due to contamination that might occur with atmospheric moisture or crystal water [61].

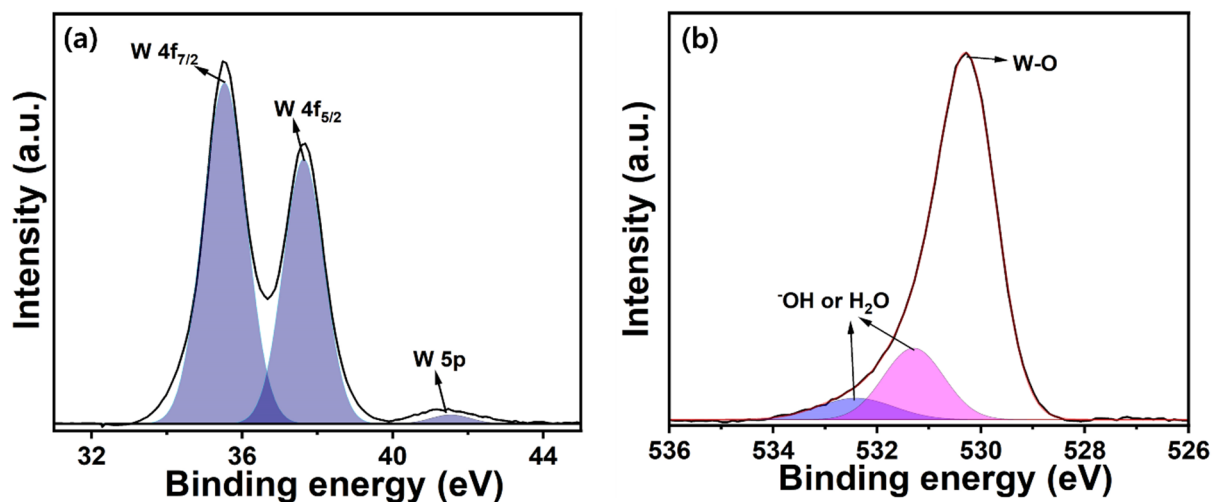


Figure 5. W 4f (a) and O 1s (b) XPS plots of HFCVD-grown WO₃ NW thin films.

3.5. Sensing Parameters of WO₃ NW Thin-Film-Based Electrodes

A HFCVD-grown WO₃ NW thin film-modified electrode is employed for the detection of methylamine. The electrochemical sensing studies were performed in 0.1 M phosphate buffer solution (PBS, pH = 7). Cyclic voltammetry (CV) measurements were used to analyze the electrochemical behavior at a scan rate of 50 mVs^{-1} . The CV graphs for the detection of methylamine are shown in Figure 6a, exhibiting a promising electrochemical reversibility and efficiency with a redox response (oxidation and reduction) of the WO₃ NW thin-film electrode of 0.2303 V redox potential [62]. These peaks usually occur due to the transfer

of electrons displaying, the oxidation peak as a result of electron-losing behavior and the reduction peak occurs due to the electron-gaining behavior. In our work, the detection of methylamine by the HFCVD-grown WO_3 NW thin-film electrode exhibits efficient electrochemical sensing behavior, which might be due to the high conductivity [33] and large surface area [63] of WO_3 NW thin films. From linear sweep voltammetry, as shown in Figure 6b, a low current value of $\sim 1.3 \mu\text{A}$ is observed in pristine PBS. However, it has been observed that upon the addition of the lowest amount of methylamine ($20 \mu\text{M}$), there is a significant change in current due to the high sensing properties of the HFCVD-grown WO_3 NW thin film. Electrolytes with different concentrations of methylamine ($20 \mu\text{M}$ – 1 mM) display a lower current response of $\sim 14.15 \mu\text{A}$ and the highest current value of $\sim 23.23 \mu\text{A}$. This gradual increase in the current indicates the rapid sensing response of HFCVD-grown WO_3 NW thin-film electrodes in the detection of methylamine, which might result from the better electrocatalytic or electrochemical behavior and the fast electron exchange of HFCVD-grown WO_3 NW thin films [64]. The increase in current upon the further addition of the targeted chemical in an electrolyte usually results in an increase in the ionic strength of the electrolyte. Herein, when increasing the methylamine concentration in the 0.1 M PBS, a large number of ions are generated; due to this response, more electrons are exchanged and this increases the opportunity for electron transfer at the electrode surface. As such, there is an increase in the rate of reaction, which enhances the sensitivity of the electrode. This result suggests that HFCVD-grown WO_3 NWs show effective sensing capabilities in the detection of methylamine [65].

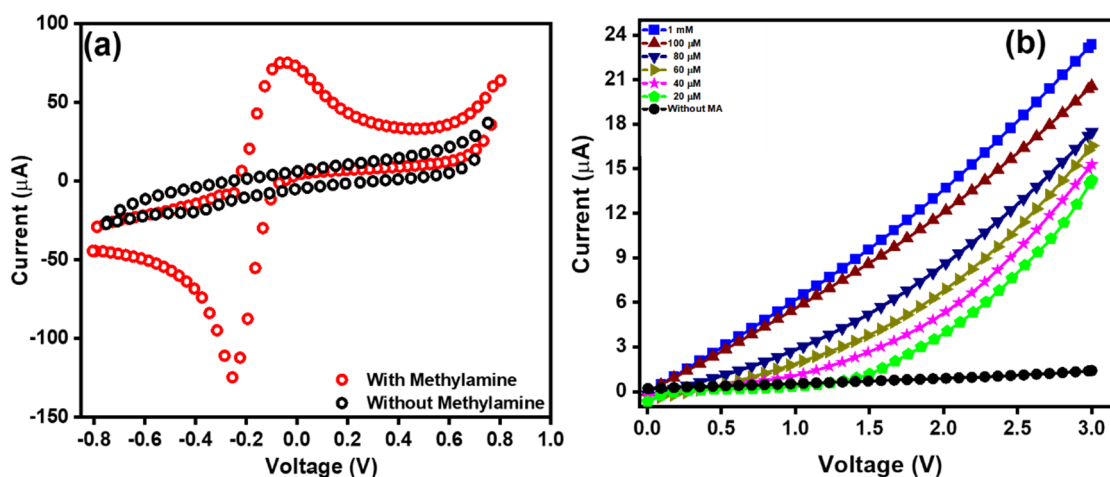


Figure 6. (a) Cyclic voltammogram plot with methylamine (1 mM) in 0.1 M PBS of a HFCVD-grown nanostructured WO_3 thin film and (b) I–V curves of the HFCVD-grown nanostructured WO_3 thin-film-based chemical.

To examine the sensitivity of HFCVD-grown WO_3 NW thin-film-based electrodes, Figure 7a shows the current vs. concentration calibration curve [33]. Herein, the current increases linearly with an increase in analyte concentration. The HFCVD-deposited WO_3 NW thin-film-based electrode shows a reproducible, reliable and considerable promising sensitivity of $\sim 183.65 \mu\text{A mM}^{-1} \text{ cm}^{-2}$ with a linearity of $20 \mu\text{M}^{-1} \text{ mM}$, a detection limit of $\sim 20 \mu\text{M}$ and a correlation coefficient (R^2) of ~ 0.97708 in 10 s response time. The existence of a good current response and reliable sensitivity might suggest high electron mobility and electrochemical activity [66] over the surface of HFCVD-grown WO_3 NW thin-film electrodes. The stability performance of HFCVD-grown WO_3 NW thin-film electrode materials was performed by a linear sweep voltammetry graph (current vs. voltage graph) in the presence of $20 \mu\text{M}$ methylamine. The electrochemical behavior was studied twice a day for 1 month. As seen in Figure 7b, $\sim 95\%$ of the current response remains the same as compared to the measurements performed on the first day of the analysis and no significant change in current is observed, which shows the good stability of HFCVD-grown WO_3 NW

thin-film electrodes. The performance of HFCVD-grown WO_3 NW thin-film-based sensor is compared to other reported sensors [67–71], as shown in Table 1.

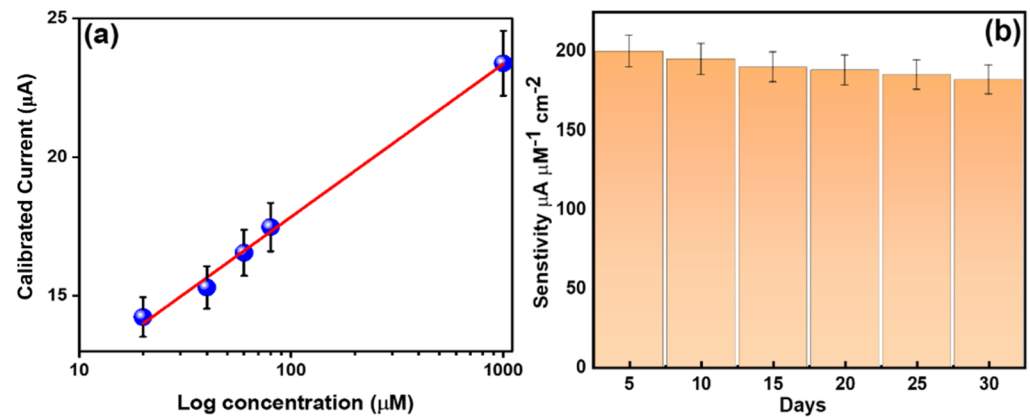
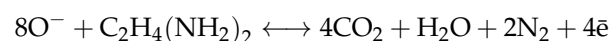
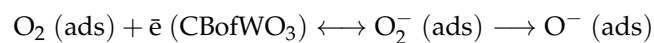
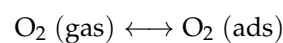


Figure 7. (a) Calibrated current versus the concentration of methylamine of HFCVD-grown WO_3 NW thin-film-based chemical sensors. (b) Stability test through I–V measurements in the presence of 20 μM methylamine in 0.1 M PBS.

Table 1. Sensing parameters of WO_3 NWs electrode-based sensors compared with reported chemical sensors.

Materials	Preparation Method	Chemicals	Sensitivity	LOD	R^2	Refs.
WO_3	HFCVD	ethylenediamine	$161.33 \mu\text{A} \mu\text{M}^{-1} \text{cm}^{-2}$	9.56 μM	0.98	[33]
PANI/Gr	Spin coating	hydrazine	$32.54 \times 10^{-5} \mu\text{A} \text{cm}^{-2} \text{mM}^{-1}$	15.38 mM	0.78578	[38]
Ag_2O	Sonochemical method	acetone	$1.689 \mu\text{A} \text{cm}^{-2} \text{mM}^{-1}$	0.11 μM	0.946	[67]
Ce_2O_3	Wet chemical method	2-nitrophenol	$1.689 \mu\text{A} \text{mM}^{-1} \text{cm}^{-2}$		0.9030	[68]
WO_3	HFCVD	diethylamine	$3.5 \mu\text{A} \mu\text{M}^{-1} \text{cm}^{-2}$	7 μM		[69]
ZnFe_2O_4	Hydrothermal method	formaldehyde	$4.10 \mu\text{A} \text{cm}^{-2} \text{mM}^{-1}$	0.89 μM		[70]
MAPbBr_3	Electrospun	methylamine	-	0.8 ppm	0.9904	[71]
WO_3	HFCVD	methylamine	$183.65 \mu\text{A} \mu\text{M}^{-1} \text{cm}^{-2}$	20 μM	0.97708	This work

The detection mechanism of methylamine by HFCVD-grown WO_3 NW thin-film-based electrodes is related to the changes in electrode conductance during the interaction of fabricated electrodes with an analyte. As shown in Figure 8, oxygen species adhere to the surface of WO_3 NW thin films grown through the HFCVD process. The HFCVD-grown WO_3 NW thin film shows n-type semiconducting behavior [33]. Due to the nature of WO_3 thin films, electrons in the conduction band tend to bond with the surface area of WO_3 thin films. By capturing electrons within WO_3 thin films, these oxygen species (O_2 adsorbed) transform into active sites, converting into anionic species containing oxygen [72]. The presence of these adsorbed oxygen species on the surface stimulates low-energy electrons in the valence band, leading to an increase in the number of holes within the HFCVD-grown WO_3 NW thin film. This accumulation of holes eventually results in reduced resistance in the fabricated sensor. When the target methylamine molecule interacts with the adsorbed oxygen ions, it triggers the release of trapped electrons, as described by the following equations:



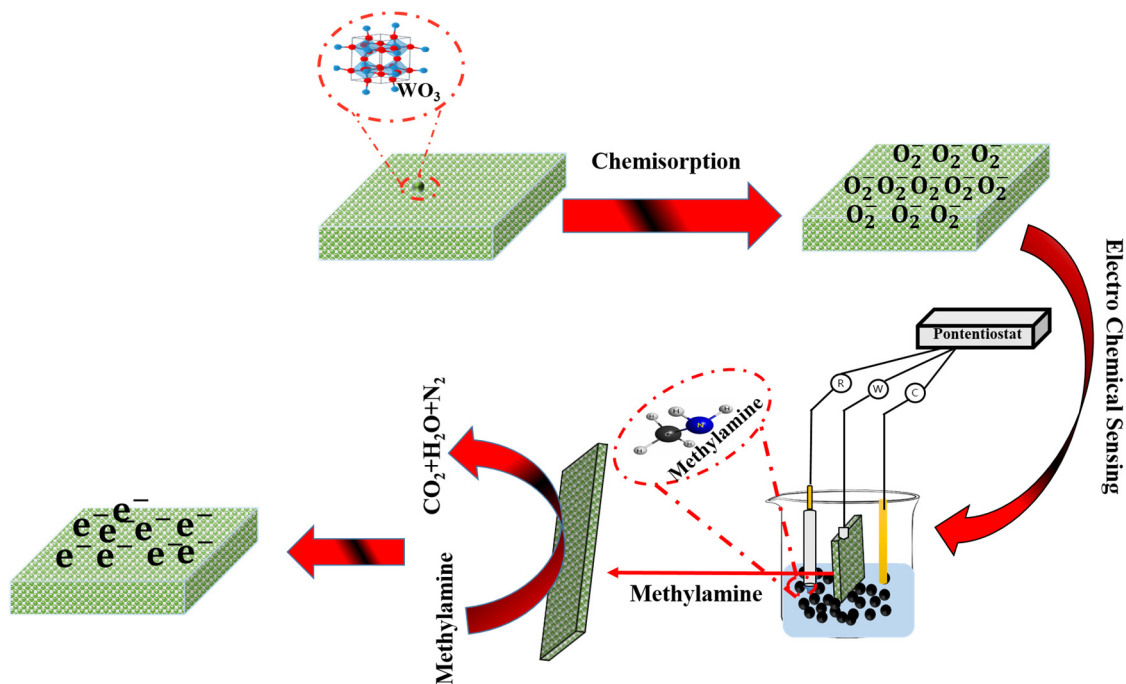


Figure 8. Possible sensing mechanism for the detection of methylamine over the surface of HFCVD-grown WO_3 NW thin-film-based electrodes.

During the oxidation process, electrons emitted from the conduction band of the HFCVD-grown WO_3 thin-film NWs enhance the electrical conductivity, resulting in an increased current associated with the methylamine [73]. In our work, the deposited WO_3 thin film exhibits uniformly distributed nanowalls of an average grain size of $\sim 20\text{--}25$ nm. This structure might provide a large surface area for adsorption, making it highly efficient for the detection of methylamine, ensuring exceptional electrochemical performance.

4. Conclusions

This study focuses on the development of a sensitive sensor for detecting the hazardous chemical methylamine. A uniform WO_3 thin-film nanowall structure on a Si substrate is obtained at a relatively low temperature of ~ 400 °C through HFCVD. The resulting WO_3 NW-based thin-film-based electrode exhibits highly effective detection of methylamine at very low concentrations. The obtained results are attributed to the unique nanowall-like structure of WO_3 thin films, which might offer a large surface area, facilitating efficient electron transfer during the electrochemical detection of methylamine. The WO_3 NW-based fabricated chemical sensor demonstrates a promising sensitivity of $\sim 196.33 \mu\text{A} \mu\text{M}^{-1} \text{cm}^{-2}$, a low limit of detection (LOD) of $\sim 12 \mu\text{M}$, and a strong retention coefficient of ~ 0.97708 . Thus, our fabricated sensor has the potential for application in environmental monitoring, making it adaptable for the detection of other harmful chemicals in the future.

Author Contributions: Conceptualization, M.I. and E.-B.K.; methodology, M.I.; software, M.I., D.-H.K., T.-G.K. and E.-B.K.; validation, M.I., M.S.A. and E.-B.K.; formal analysis, M.I. and E.-B.K.; investigation, M.I.; resources, M.I. and T.-G.K.; data curation, M.I., E.-B.K. and S.A.; writing—original draft preparation, M.I. and E.-B.K.; writing—review and editing, M.S.A. and S.A.; supervision, S.A.; project administration, M.S.A. and D.-H.K.; funding acquisition, M.S.A., D.-H.K. and E.-B.K. All authors have read and agreed to the published version of the manuscript.

Funding: This research was supported by National University Development Project at Jeonbuk National University in 2022.

Data Availability Statement: The original contributions presented in the study are included in the article, further inquiries can be directed to the corresponding authors.

Conflicts of Interest: The authors declare no conflicts of interest.

References

1. Theerthagiri, J.; Chandrasekaran, S.; Salla, S.; Elakkiya, V.; Senthil, R.A.; Nithyadharseni, P.; Maiyalagan, T.; Micheal, K.; Ayeshamariam, A.; Arasu, M.V.; et al. Recent Developments of Metal Oxide Based Heterostructures for Photocatalytic Applications towards Environmental Remediation. *J. Solid State Chem.* **2018**, *267*, 35–52. [[CrossRef](#)]
2. Kanazawa, E.; Sakai, G.; Shimanoe, K.; Kanmura, Y.; Teraoka, Y.; Miura, N.; Yamazoe, N. Metal Oxide Semiconductor N₂O Sensor for Medical Use. *Sens. Actuators B Chem.* **2001**, *77*, 72–77. [[CrossRef](#)]
3. Li, F.; Ran, J.; Jaroniec, M.; Qiao, S.Z. Solution Combustion Synthesis of Metal Oxide Nanomaterials for Energy Storage and Conversion. *Nanoscale* **2015**, *7*, 17590–17610. [[CrossRef](#)] [[PubMed](#)]
4. Bashambu, L.; Singh, R.; Verma, J. Metal/Metal Oxide Nanocomposite Membranes for Water Purification. *Mater. Today Proc.* **2021**, *44*, 538–545. [[CrossRef](#)]
5. Jolly, A.; Kim, H.; Moon, J.-Y.; Mohan, A.; Lee, Y.-C. Exploring the Imminent Trends of Saponins in Personal Care Product Development: A Review. *Ind. Crops Prod.* **2023**, *205*, 117489. [[CrossRef](#)]
6. Sun, Y.-F.; Liu, S.-B.; Meng, F.-L.; Liu, J.-Y.; Jin, Z.; Kong, L.-T.; Liu, J.-H. Metal Oxide Nanostructures and Their Gas Sensing Properties: A Review. *Sensors* **2012**, *12*, 2610–2631. [[CrossRef](#)] [[PubMed](#)]
7. Subramani, T.; Thimmarayan, G.; Balraj, B.; Chandrasekar, N.; Palanisamy, M.; Nagarajan, S.K.; Amirtharajan, S.; Kumar, M.; Sivakumar, C. Surfactants Assisted Synthesis of WO₃ Nanoparticles with Improved Photocatalytic and Antibacterial Activity: A Strong Impact of Morphology. *Inorg. Chem. Commun.* **2022**, *142*, 109709. [[CrossRef](#)]
8. Diez-Cabanes, V.; Segalina, A.; Pastore, M. Effects of Size and Morphology on the Excited-State Properties of Nanoscale WO₃ Materials from First-Principles Calculations: Implications for Optoelectronic Devices. *ACS Appl. Nano Mater.* **2022**, *5*, 16289–16297. [[CrossRef](#)]
9. Lima, L.V.C.; Rodriguez, M.; Freitas, V.A.A.; Souza, T.E.; Machado, A.E.H.; Patrocínio, A.O.T.; Fabris, J.D.; Oliveira, L.C.A.; Pereira, M.C. Synergism between n-type WO₃ and p-type δ-FeOOH semiconductors: High interfacial contacts and enhanced photocatalysis. *Appl. Catal. B Environ.* **2015**, *165*, 579–588. [[CrossRef](#)]
10. Azam, A.; Kim, J.; Park, J.; Novak, T.G.; Tiwari, A.P.; Song, S.H.; Kim, B.; Jeon, S. Two-Dimensional WO₃ Nanosheets Chemically Converted from Layered WS₂ for High-Performance Electrochromic Devices. *Nano Lett.* **2018**, *18*, 5646–5651. [[CrossRef](#)]
11. Jadkar, V.; Pawbake, A.; Waykar, R.; Jadhavar, A.; Date, A.; Late, D.; Pathan, H.; Gosavi, S.; Jadkar, S. Synthesis of g-WO₃ thin films by hot wire-CVD and investigation of its humidity sensing properties. *Phys. Status Solidi A* **2017**, *214*, 1600717. [[CrossRef](#)]
12. Godbole, R.; Godbole, V.; Bhagwat, S. Palladium enriched tungsten oxide thin films: An efficient gas sensor for hazardous gases. *Eur. Phys. J. B* **2019**, *92*, 78. [[CrossRef](#)]
13. Zhu, L.; Zheng, W. Room-temperature gas sensing of ZnO-based gas sensor: A review. *Sens. Actuators A Phys.* **2017**, *267*, 242–261. [[CrossRef](#)]
14. Zou, Y.S.; Zhang, Y.C.; Lou, D.; Wang, H.P.; Gu, L.; Dong, Y.H.; Dou, K.; Song, X.F.; Zeng, H.B. Structural and optical properties of WO₃ films deposited by pulsed laser deposition. *J. Alloys Compd.* **2014**, *583*, 465–470. [[CrossRef](#)]
15. Heidari, E.K.; Zamani, C.; Marzbanrad, E.; Raissi, B.; Nazarpour, S. WO₃-based NO₂ sensors fabricated through low frequency AC electrophoretic deposition. *Sens. Actuators B Chem.* **2010**, *146*, 165–170. [[CrossRef](#)]
16. Kim, T.S.; Kim, Y.B.; Yoo, K.S.; Sung, G.S.; Jung, H.J. Sensing characteristics of dc reactive sputtered WO₃ thin films as an NO_x gas sensor. *Sens. Actuators B Chem.* **2000**, *62*, 102–108. [[CrossRef](#)]
17. Arutanti, O.; Ogi, T.; Nandiyanto, A.B.D.; Iskandar, F.; Okuyama, K. Controllable crystallite and particle sizes of WO₃ particles prepared by a spray-pyrolysis method and their photocatalytic activity. *Inorg. Mater. Synth. Process.* **2014**, *60*, 41–49. [[CrossRef](#)]
18. Li, Y.; McMaster, W.A.; Wei, H.; Chen, D.; Caruso, R.A. Enhanced Electrochromic Properties of WO₃ Nanotree-like Structures Synthesized via a Two-Step Solvothermal Process Showing Promise for Electrochromic Window Application. *ACS Appl. Nano Mater.* **2018**, *1*, 2552–2558. [[CrossRef](#)]
19. Su, X.; Xiao, F.; Li, Y.; Jian, J.; Sun, Q.; Wang, J. Synthesis of uniform WO₃ square nanoplates via an organic acid-assisted hydrothermal process. *Mater. Lett.* **2010**, *64*, 1232–1234. [[CrossRef](#)]
20. Salmaoui, S.; Sediri, F.; Gharbi, N. Characterization of h-WO₃ nanorods synthesized by hydrothermal process. *Polyhedron* **2010**, *29*, 1771–1775. [[CrossRef](#)]
21. Djaoued, Y.; Priya, S.; Balaji, S. Low temperature synthesis of nanocrystalline WO₃ films by sol-gel process. *J. Non-Cryst. Solids* **2008**, *354*, 673–679.
22. Kafizas, A.; Francàs, L.; Sotelo-Vazquez, C.; Ling, M.; Li, Y.; Glover, E.; McCafferty, L.; Blackman, C.; Darr, J.; Parkin, I. Optimizing the Activity of Nanoneedle Structured WO₃ Photoanodes for Solar Water Splitting: Direct Synthesis via Chemical Vapor Deposition. *J. Phys. Chem. C* **2017**, *121*, 5983–5993. [[CrossRef](#)]
23. Keshri, S.; Kumar, A.; Kabiraj, D. Effect of Annealing on Structural, Optical and Electrical Behaviors of WO₃ Thin Films Prepared by Physical Vapor Deposition Method. *J. Nano-Electron. Phys.* **2011**, *3*, 260–267.
24. Buch, V.R.; Chawla, A.K.; Rawal, S.K. Review on electrochromic property for WO₃ thin films using different deposition techniques. *Mater. Today Proc.* **2016**, *3*, 1429–1437. [[CrossRef](#)]
25. Godbole, R.; Ameen, S.; Nakate, U.T.; Akhtar, M.S.; Shin, H.-S. Low temperature HFCVD synthesis of tungsten oxide thin film for high response hydrogen gas sensor application. *Mater. Lett.* **2019**, *19*, 398–401. [[CrossRef](#)]

26. Zhai, Z.; Shen, H.; Chen, J.; Li, X.; Jiang, Y. Evolution of Structural and Electrical Properties of Carbon Films from Amorphous Carbon to Nanocrystalline Graphene on Quartz Glass by HFCVD. *ACS Appl. Mater. Interfaces* **2018**, *10*, 17427–17436. [[CrossRef](#)] [[PubMed](#)]
27. Zhang, T.; Zou, Y. The Effect of Deposition Parameters on the Growth Rate of Microcrystalline Diamond Powders Synthesized by HFCVD Method. *Coating* **2017**, *7*, 95. [[CrossRef](#)]
28. Tan, G.L.; Tang, D.; Dastan, D.; Jafari, A.; Silva, J.P.B.; Yin, X.T. Effect of heat treatment on electrical and surface properties of tungsten oxide thin films grown by HFCVD technique. *Mater. Sci. Semicon. Process.* **2021**, *122*, 105506. [[CrossRef](#)]
29. Jacob, S.P.C. The influence of substrate temperature variation on tungsten oxide thin film growth in an HFCVD system. *Appl. Surf. Sci.* **2007**, *253*, 3317–3325.
30. Jafari, A.; Ghoranneviss, M.; Elahi, A.S. HFCVD application for growth of monoclinic tungsten trioxide crystal nano-walls. *J. Inorg. Organomet. Polym. Mater.* **2016**, *26*, 254–258. [[CrossRef](#)]
31. White, C.M.; Gillaspie, D.T.; Whitney, E.; Lee, S.-H.; Dillon, A.C. Flexible electrochromic devices based on crystalline WO₃ nanostructures produced with hot-wire chemical vapor deposition. *Thin Solid Films* **2009**, *517*, 3596–3599. [[CrossRef](#)]
32. Shankar, N.; Yu, M.-F.; Vanka, S.P.; Glumac, N.G. Synthesis of tungsten oxide (WO₃) nanorods using carbon nanotubes as templates by hot filament chemical vapor deposition. *Mater. Lett.* **2006**, *60*, 771–774. [[CrossRef](#)]
33. Imran, M.; Kim, E.-B.; Kwak, D.-H.; Akhtar, M.S.; Ameen, S. Controlled Growth of WO₃ Pyramidal Thin Film via Hot-Filament Chemical Vapor Deposition: Electrochemical Detection of Ethylenediamine. *Chemosensors* **2021**, *9*, 257. [[CrossRef](#)]
34. Lu, D.; Ogino, A.; Liang, B.; Liu, J.; Nagatsu, M. Field-Emission Properties of Nanostructured WO₃ Arrays Fabricated Using Tungsten Hot-Filament Chemical Vapor Deposition. *Jpn. J. Appl. Phys.* **2009**, *48*, 090206. [[CrossRef](#)]
35. Sahu, C.; Sircar, A.; Sangwai, J.S.; Kumar, R. Effect of Methylamine, Amylamine, and Decylamine on the Formation and Dissociation Kinetics of CO₂ Hydrate Relevant for Carbon Dioxide Sequestration. *Ind. Eng. Chem. Res.* **2022**, *61*, 2672–2684. [[CrossRef](#)]
36. Vinogradoff, V.; Duvernay, F.; Danger, G.; Theulé, P.; Borget, F.; Chiavassa, T. Formaldehyde and methylamine reactivity in interstellar ice analogues as a source of molecular complexity at low temperature. *Astron. Astrophys.* **2013**, *549*, A40. [[CrossRef](#)]
37. Noorhashimah, M.N.; Razak, K.A.; Lockman, Z. Effect of Concentration and pH of PBS to the Electrocatalytic Performance of Enzymatic Glucose Biosensor. *Solid State Phenom.* **2019**, *290*, 195–198. [[CrossRef](#)]
38. Murugappan, K.; Kang, C.; Silvester, D.S. Electrochemical Oxidation and Sensing of Methylamine Gas in Room Temperature Ionic Liquids. *J. Phys. Chem. C* **2014**, *118*, 19232–19237. [[CrossRef](#)]
39. Dai, X.; Rabeah, J.; Yuan, H.; Brückner, A.; Cui, X.; Shi, F. Glycerol as a Building Block for Prochiral Aminoketone, N-Formamide, and N-Methyl Amine Synthesis. *ChemSusChem* **2016**, *9*, 3133–3138. [[CrossRef](#)]
40. Liu, Y.; Xu, X.; Lu, H.; Yan, B. Dual-emission ratiometric fluorescent probe-based lanthanide-functionalized hydrogen-bonded organic framework for the visual detection of methylamine. *J. Mater. Chem. C* **2022**, *10*, 1212–1219. [[CrossRef](#)]
41. Huang, G.; Zhou, Y.; Li, F.; Tan, X.; Cai, Z.; Luo, D.; Chen, T.; Zhang, M. An effective and reliable fluorescent sensor for selective detection of methylamine gas based on in-situ formation of MAPbBr₃ perovskite nanocrystals in electrospun fibers. *Sens. Actuators B Chem.* **2021**, *347*, 130618. [[CrossRef](#)]
42. Kim, T.-H.; Yoon, J.-W.; Kang, Y.C.; Abdel-Hady, F.; Wazzan, A.A.; Lee, J.-H. A strategy for ultrasensitive and selective detection of methylamine using p-type Cr₂O₃: Morphological design of sensing materials, control of charge carrier concentrations, and configurational tuning of Au catalysts. *Sens. Actuators B Chem.* **2017**, *240*, 1049–1057. [[CrossRef](#)]
43. Rajagopal, S.; Nataraj, D.; Mangalaraj, D.; Djaoued, Y.; Robichaud, J.; Khyzhun, O.Y. Controlled Growth of WO₃ Nanostructures with Three Different Morphologies and Their Structural, Optical, and Photodecomposition Studies. *Nanoscale Res. Lett.* **2009**, *4*, 1335–1342. [[CrossRef](#)] [[PubMed](#)]
44. Phuruangrat, A.; Ham, D.J.; Hong, S.J.; Thongtem, S.; Lee, J.S. Synthesis of hexagonal WO₃ nanowires by microwave-assisted hydrothermal method and their electrocatalytic activities for hydrogen evolution reaction. *J. Mater. Chem.* **2010**, *20*, 1780–1786. [[CrossRef](#)]
45. Hunge, Y.M.; Yadav, A.A.; Mathe, V.L. Ultrasound assisted synthesis of WO₃-ZnO nanocomposites for brilliant blue dye degradation. *Ultrason. Sonochem.* **2018**, *45*, 116–122. [[CrossRef](#)] [[PubMed](#)]
46. Hersh, H.N.; Kramer, W.E.; McGee, J.H. Mechanism of electrochromism in WO₃. *Appl. Phys. Lett.* **1975**, *27*, 646–648. [[CrossRef](#)]
47. González-Borrero, P.P.; Sato, F.; Medina, A.N.; Baesso, M.L.; Bento, A.C.; Baldissera, G.; Persson, C.; Niklasson, G.A.; Granqvist, C.G.; Ferreira da Silva, A. Optical band-gap determination of nanostructured WO₃ film. *Appl. Phys. Lett.* **2010**, *96*, 061909. [[CrossRef](#)]
48. Vemuri, R.S.; Engelhard, M.H.; Ramana, C.V. Correlation between Surface Chemistry, Density, and Band Gap in Nanocrystalline WO₃ Thin Films. *ACS Appl. Mater. Interfaces* **2012**, *4*, 1371–1377. [[CrossRef](#)]
49. Colton, R.J.; Guzman, A.M.; Rabalais, J.W. Electrochromism in some thin-film transition-metal oxides characterized by X-ray electron spectroscopy. *J. Appl. Phys.* **1978**, *49*, 409–416. [[CrossRef](#)]
50. Daniel, M.F.; Desbat, B.; Lassegues, J.C.; Gerand, B.; Figlarz, M. Infrared and Raman study of WO₃ tungsten trioxides and WO₃·xH₂O tungsten trioxide hydrates. *J. Solid State Chem.* **1987**, *67*, 235–247. [[CrossRef](#)]
51. Lee, S.H.; Cheong, H.M.; Liu, P.; Smith, D.; Tracy, C.E.; Mascarenhas, A.; Pitts, J.R.; Deb, S.K. Raman spectroscopic studies of gasochromic a-WO₃ thin films. *Electrochim. Acta* **2011**, *46*, 1995–1999. [[CrossRef](#)]

52. Boulova, M.; Lucazeau, G. Crystallite Nanosize Effect on the Structural Transitions of WO₃ Studied by Raman Spectroscopy. *J. Solid State Chem.* **2002**, *167*, 425–434. [[CrossRef](#)]
53. Cazzanelli, E.; Vinegoni, C.; Mariotto, G.; Kuzmin, A.; Purans, J. Raman study of the phase transitions sequence in pure WO₃ at high temperature and in HxWO₃ with variable hydrogen content. *Solid State Ionics* **1999**, *123*, 67–74. [[CrossRef](#)]
54. Kanan, S.M.; Tripp, C.P. Synthesis, FTIR studies and sensor properties of WO₃ powders. *Curr. Opin. Solid State Mater. Sci.* **2007**, *11*, 19–27. [[CrossRef](#)]
55. Deepa, M.; Sharma, N.; Varshney, P.; Varma, S.P.; Agnihotry, S.A. FTIR investigations of solid precursor materials for sol-gel deposition of WO₃ based electrochromic films. *J. Mater. Sci.* **2000**, *35*, 5313–5318. [[CrossRef](#)]
56. Charton, P.; Gengembre, L.; Armand, P. TeO₂-WO₃ Glasses: Infrared, XPS and XANES Structural Characterizations. *J. Solid State Chem.* **2002**, *168*, 175–183. [[CrossRef](#)]
57. Shpak, A.P.; Korduban, A.M.; Medvedskij, M.M.; Kandyba, V.O. XPS studies of active elements surface of gas sensors based on WO_{3-x} nanoparticles. *J. Electron Spectrosc. Relat. Phenom.* **2007**, *156–158*, 172–175.
58. Lozzi, L.; Ottaviano, L.; Passacantando, M.; Santucci, S.; Cantalini, C. The influence of air and vacuum thermal treatments on the NO₂ gas sensitivity of WO₃ thin films prepared by thermal evaporation. *Thin Solid Films* **2001**, *391*, 224–228. [[CrossRef](#)]
59. Leftheriotis, G.; Papaefthimiou, S.; Yianoulis, P.; Siokou, A. Effect of the tungsten oxidation states in the thermal coloration and bleaching of amorphous WO₃ films. *Thin Solid Films* **2001**, *384*, 298–306. [[CrossRef](#)]
60. Soto, G.; De La Cruz, W.; Díaz, J.A.; Machorro, R.; Castellón, F.F.; Fariás, M.H. Characterization of tungsten oxide films produced by reactive pulsed laser deposition. *Appl. Surf. Sci.* **2003**, *218*, 281–289. [[CrossRef](#)]
61. Wang, Q.; Wu, H.; Wang, Y.; Li, J.; Yang, Y.; Cheng, X.; Luo, Y.; An, B.; Pan, X.; Xie, E. Ex-situ XPS analysis of yolk-shell Sb₂O₃/WO₃ for ultra-fast acetone resistive sensor. *J. Hazard Mater.* **2021**, *412*, 125175. [[CrossRef](#)]
62. Joshi, N.; da Silva, L.F.; Jadhav, H.S.; Shimizu, F.M.; Suman, P.H.; M'Peko, J.C.; Orlandie, M.O.; Seo, J.G.; Mastelaro, V.R.; Oliveira, O.N., Jr. Yolk-shelled ZnCo₂O₄ microspheres: Surface properties and gas sensing application. *Sens. Actuators B Chem.* **2018**, *257*, 906–915. [[CrossRef](#)]
63. Kim, E.-B.; Imran, M.; Shaheer Akhtar, M.; Shin, H.-S.; Ameen, S. Enticing 3D peony-like ZnGa₂O₄ microstructures for electrochemical detection of N, N-dimethylmethanamide chemical. *J. Hazard. Mater.* **2021**, *404*, 124069. [[CrossRef](#)]
64. Imran, M.; Kim, E.-B.; Kwak, D.-H.; Ameen, S. Porous MgNiO₂ Chrysanthemum Flower Nanostructure Electrode for Toxic Hg²⁺ Ion Monitoring in Aquatic Media. *Sensors* **2023**, *23*, 7910. [[CrossRef](#)] [[PubMed](#)]
65. Li, N.; Fan, Y.; Shi, Y.; Xiang, Q.; Wang, X.; Xu, J. A low temperature formaldehyde gas sensor based on hierarchical SnO/SnO₂ nano-flowers assembled from ultrathin nanosheets: Synthesis, sensing performance and mechanism. *Sens. Actuators B Chem.* **2019**, *294*, 106–115. [[CrossRef](#)]
66. Ibrahim, A.A.; Dar, G.N.; Zaidi, S.A.; Umar, A.; Abaker, M.; Bouzid, H.; Baskoutas, S. Growth and properties of Ag-doped ZnO nanoflowers for highly sensitive phenyl hydrazine chemical sensor application. *Talanta* **2012**, *93*, 257–263. [[CrossRef](#)]
67. Murugappan, K.; Silvester, D.S. Sensors for Highly Toxic Gases: Methylamine and Hydrogen Chloride Detection at Low Concentrations in an Ionic Liquid on Pt Screen Printed Electrodes. *Sensors* **2015**, *15*, 26866–26876. [[CrossRef](#)] [[PubMed](#)]
68. Rahman, M.M.; Khan, S.B.; Jamal, A.; Faisal, M.; Asiri, A.M. Fabrication of highly sensitive acetone sensor based on sonochemically prepared as-grown Ag₂O nanostructures. *Chem. Eng. J.* **2012**, *192*, 122–128. [[CrossRef](#)]
69. Hussain, M.M.; Rahman, M.M.; Asiri, A.M. Efficient 2-Nitrophenol Chemical Sensor Development Based on Ce₂O₃ Nanoparticles Decorated CNT Nanocomposites for Environmental Safety. *PLoS ONE* **2016**, *11*, e0166265. [[CrossRef](#)] [[PubMed](#)]
70. Godbole, R.; Imran, M.; Kim, E.-B.; Park, J.B.; Ameen, S. Novel approach to synthesize morphology variant tungsten oxide thin films for efficient chemical sensing. *Ceram. Int.* **2022**, *48*, 12506–12514. [[CrossRef](#)]
71. Rahman, M.; Khan, S.B.; Faisal, M.; Asiri, A.M.; Alamry, K.A. Highly sensitive formaldehyde chemical sensor based on hydrothermally prepared spinel ZnFe₂O₄ nanorods. *Sens. Actuators B Chem.* **2012**, *171*, 932–937. [[CrossRef](#)]
72. Kim, E.B.; Ameen, S.; Akhtar, M.S.; Shin, H.S. Iron-nickel co-doped ZnO nanoparticles as scaffold for field effect transistor sensor: Application in electrochemical detection of hexahydropyridine chemical. *Sens. Actuators B Chem.* **2018**, *275*, 422–431. [[CrossRef](#)]
73. Ameen, S.; Akhtar, M.S.; Shin, H.S. Hydrazine chemical sensing by a modified electrode based on in situ electrochemically synthesized polyaniline/graphene composite thin film. *Sens. Actuators B Chem.* **2012**, *173*, 177–183. [[CrossRef](#)]

Disclaimer/Publisher's Note: The statements, opinions and data contained in all publications are solely those of the individual author(s) and contributor(s) and not of MDPI and/or the editor(s). MDPI and/or the editor(s) disclaim responsibility for any injury to people or property resulting from any ideas, methods, instructions or products referred to in the content.